

Modelling the Strong Coupling of Excitons to Cavity Photons in Cuprous Oxide (Cu_2O)

Fredrik Johannes Olsen Hasselgren

June 17, 2024

Abstract

Exciton-Polaritons are quasiparticles formed from the strong coupling of excitons and photons [1]. An exciton is an electron and hole held together by the Coulomb interaction in a semiconductor [1, 2]. In a recent study at the University of St Andrews, a thin crystal of cuprous oxide (Cu_2O) underwent high resolution spectroscopy [3]. Excitonic peaks in the absorption spectrum were identified for principal quantum number $n = 2, 3, \dots, 12$, with the presence of exciton-polaritons demonstrated for $n = 3, 4, \dots, 6$ [3]. In the present model-based analysis peak energies, linewidths, and oscillator strengths were extracted from the paper’s empirical data. Additionally, the optical setup was simulated using the Transfer Matrix Method, built on code from the study, to investigate the linewidth of the cavity itself. Using these parameters, a coupled oscillator model was built, coupling 11 excitons to the cavity photon, to investigate the system’s eigenenergies, eigenvectors, and polariton intensities. The model demonstrates how increasing the cavity linewidth obstructs the identification of polariton splittings, whilst decreasing linewidths or increasing coupling strengths creates more splittings. Finally, the imaginary part of the refractive index of Cu_2O is used to model an energy dependent cavity linewidth, further obstructing higher order polariton formation. Thus, the model is capable of explaining the discrepancy between the number of excitons and the number of polaritons experimentally found in [3].

1 Introduction

Excitons are formed when light is absorbed by the semiconductor, promoting an electron from the valence band to the conduction band [4]. The promotion creates the quasiparticle called the electron-hole in the valence band, similar to an electron with opposite charge, momentum, and a different effective

mass [5, 6]. As such, the Coulomb-bound electron - electron-hole pair is a bosonic quasiparticle made up of two charged fermions [5, 7]. The exciton can decay by emitting a photon of energy equal to the energy difference between the two bands, due to the electron and electron-hole’s wave functions overlapping sufficiently for their recombination [5, 8].

If we couple the re-emitted photon to the exciton in a reflective cavity (Fig 1 A), it may later be re-absorbed to create another exciton. This interaction between the cavity mode and the exciton can be enhanced by positioning excitons at the antinodes of the cavity [9, 10]. The strong coupling regime is reached when the rate of photons converted into excitons and vice versa exceeds the rate of photons lost to cavity imperfections together with the rate of exciton decay [1]. For exciton-polaritons the excitations of the system are no longer the exciton or photon modes, but instead new eigenmodes constituting the newly formed polaritons.

As mixed states of light and matter, exciton-polaritons have revolutionary potential as platforms for strongly interacting photons. Light, with its highly useful quantum properties, interacts too weakly for many applications, but binding it with matter which reacts strongly could circumvent this problem [11, 12]. Exciton-polaritons have already demonstrated a wide range of potentially useful phenomena like exciton-polariton condensation [6], superfluidity (a liquid with zero viscosity) [13, 14], and quantum vortices [15, 16, 17]. Recent interest in excitons and their polaritons have also included applications for logic gates in digital, optical, and quantum computing [18, 19, 11].

The coupling of multiple excitons to a cavity photon benefits greatly from modelling methods, as the complex analytical solutions quickly become unmanageable [20]. Additionally, the optical complex-

ity of components like distributed Bragg reflectors (DBRs), likewise has analytical solutions, but they are in practice often too unwieldy without extensive matrix computation [21]. Therefore the aim of this project is to employ the coupled oscillator model and the transfer matrix method to authentically model Cu_2O surrounded by DBRs, and to explore the conditions that allow and disallow the detection of excitons and their polaritons. Modelling of this kind could be a useful tool for generating polaritons with as high n as possible, working towards closing the discrepancy between the number of excitons and polaritons created.

1.1 Excitons

Excitons are the condensed-matter analogues of hydrogen atoms, with the electron-hole corresponding to the proton nucleus [22, 5]. The excitons considered for this project are the yellow series of Cu_2O formed from transitions from the uppermost valence band to the lowest conduction band [23, 24]. At large principal quantum numbers n their extensions are so large as to resemble Rydberg atoms [4, 25]. As such, the energies of the excitons approximately follow the Rydberg formula:

$$E_n = E_g - Ry/n^2 \quad (1)$$

These Rydberg excitons have longer lifetimes and stronger interactions, making them ideal for future quantum technologies [4, 26]. Kazimierczuk et al. used high resolution spectroscopy to study the formation of Rydberg excitons, measuring the transmitted intensity when shining a laser through a thin sample of cuprous oxide. Cu_2O is a direct band-gap semiconductor which allows an absorbed photon to directly create an electron-hole pair [27]. It also has a high Rydberg energy $Ry \approx 100 \text{ meV}$, making it easier to distinguish higher n excitons [4]. Kazimierczuk et al. found 25 distinct peaks corresponding to excitonic states in the optical density of Cu_2O , with giant extensions up to the order of micrometers.

The linewidths of the excitonic peaks represent the decay rate of the excitons [28, 5, 29]. These linewidths are also useful as they can be used to determine the lifetime of the exciton via employing Heisenberg's uncertainty principle (2).

$$\tau_n \approx \hbar \Gamma_n \quad (2)$$

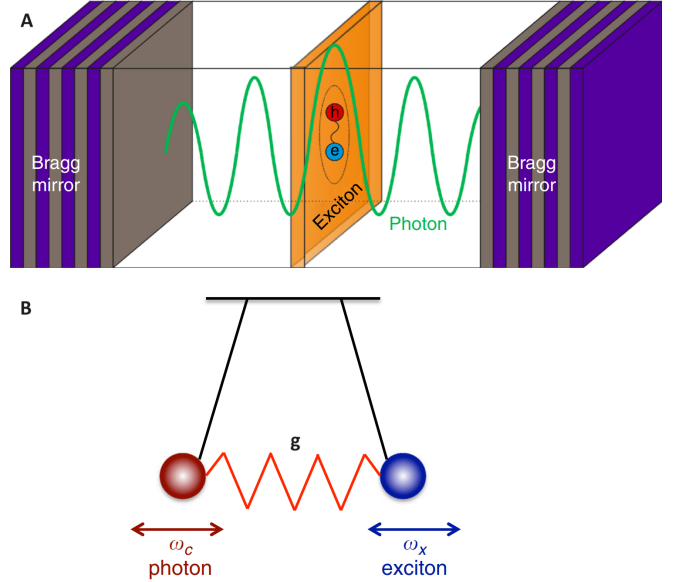


Figure 1: A: Schema of a microcavity with an exciton in the semiconductor surrounded by DBR layers, coupling it to the cavity photon. B: Schema of an exciton coupled to the cavity photons as two classical coupled oscillators at ω_c, x coupled together with strength g . Adapted from [34].

where Γ_n is the linewidth of the exciton and, τ_n is the lifetime [4].

Theoretical derivations in [30] demonstrated that due to the overlap between the initial and final exciton wavefunctions, the linewidth should scale according to n^{-3} [31]. Finally, the oscillator strength associated with each exciton is a function of selection rules determining which optical transitions are allowed via applying Fermi's golden rule [23, 32]. For P-state excitons considered in this project, theoretical derivations indicate that the oscillator strength should scale according to (3) [5, 33].

$$f_{osc} \propto \frac{n^2 - 1}{n^5} \quad (3)$$

Which means that for higher n values, the oscillator strength will also scale as n^{-3} [5].

1.2 Strong Coupling

Exciton-polaritons can be modelled as strongly coupled classical oscillators (Fig 1 B) [28]. The strong coupling regime between two oscillators occurs when their interaction is sufficiently large for the exchange to become reversible, making the overall excitation delocalized and giving the system two new eigenstates [35, 36]. These new eigenstates can be ob-

served as a splitting of the systems eigenenergies occurring where the oscillator energies meet. The strong coupling regime is reached when this splitting is greater than the sum of the linewidth of the oscillators, which corresponds to the dampening or losses associated with each oscillator [35, 37].

Classically two oscillators with eigenfrequencies $\omega_A^0 = \sqrt{(k_A/m_A)}$ and $\omega_B^0 = \sqrt{(k_B/m_B)}$ can be coupled together with coupling constant g to produce the following equations of motion [35].

$$m_A \ddot{x}_A + k_A x_A + g(x_A - x_B) = 0 \quad (4a)$$

$$m_B \ddot{x}_B + k_B x_B + g(x_A - x_B) = 0 \quad (4b)$$

These differential equations will have a solution for $x(t)$ as a function of two new eigenfrequencies ω_{\pm} [35].

$$x_i^0 \exp(-i\omega_{\pm}t) \quad (5)$$

Next, we can substitute this solution into (4), and write the system of equations as the matrix M such that [35].

$$M \begin{bmatrix} x_A^0 \\ x_B^0 \end{bmatrix} = 0 \quad (6)$$

Setting $\det(M) = 0$ yields the non-trivial solutions for this homogeneous system of equations. From solving the characteristic equation this yields:

$$\begin{aligned} \omega_{\pm}^2 &= \frac{1}{2}[\omega_A^2 + \omega_B^2 \pm \sqrt{(\omega_A^2 - \omega_B^2)^2 + 4\Gamma\omega_A\omega_B}] \\ \omega_A &= \sqrt{\frac{k_A + g}{m_A}}, \quad \omega_B = \sqrt{\frac{k_B + g}{m_B}} \\ \Gamma &= \sqrt{\frac{g/m_A \cdot g/m_B}{\omega_A\omega_B}} \end{aligned} \quad (7)$$

The resultant strong coupling can be shown by plotting the initial eigenfrequencies and the new coupled eigenfrequencies, showing a characteristic anticrossing at where $\omega_A^0 = \omega_B^0$. At the anticrossing there is a frequency splitting Ω that scales linearly with coupling strength [35] (Fig 2).

2 Modelling methods

For this project, a coupled oscillator model was developed for 11 excitons coupled to a cavity photon. This model consists of a Hamiltonian matrix,

the real eigenvalues of which relay the eigenenergies of the polaritons possible for the system. The eigenvectors represent coefficients relating the relative probabilities of the polaritons to one another. The imaginary components of this matrix account for losses in the excitons and cavity considered.

Additionally, a transfer matrix method model was developed that can model the reflectivity of the cavity's DBRs, the transmission and reflection intensities of light passing through the cavity, and the linewidth of the cavity itself. This method is derived from considering the characteristic matrix for each interface and medium of the optical system. Ultimately, a matrix describing the entire system can be determined.

Both models were coded in Python using the Numpy and Scipy packages. The models further employs experimental absorption data for Cu_2O , along with refractive index data for Cu_2O , SiO_2 , and Ta_2O_5 at various wavelengths from [3], which was interpolated for usage in the model.

2.1 The coupled oscillator matrix

The solution to the coupled oscillator model outlined by equations (4), (6), and (7) can be generalized using matrix notation [38]. For the classical case of masses oscillating on springs, we can define \mathbf{M} and \mathbf{K} matrices to represent N masses and the spring constants between them.

$$\begin{aligned} \mathbf{M} &= \begin{pmatrix} M_1 & 0 & \dots & 0 \\ 0 & M_2 & \dots & 0 \\ \vdots & \vdots & \ddots & \vdots \\ 0 & 0 & \dots & M_N \end{pmatrix} \\ \mathbf{K} &= \begin{pmatrix} K_{1,1} & K_{1,2} & \dots & K_{1,N} \\ K_{2,1} & K_{2,2} & \dots & K_{2,N} \\ \vdots & \vdots & \ddots & \vdots \\ K_{N,1} & K_{N,2} & \dots & K_{N,N} \end{pmatrix} \end{aligned} \quad (8)$$

Where $K_{i,j}$ is the coupling constant between the i -th mass and the j -th mass. Next, we can proceed similarly to (6), and relate these matrices to one another using column vectors of x coordinates (9).

$$\mathbf{M}\ddot{\mathbf{x}} = -\mathbf{K}\mathbf{x} \quad \mathbf{x} = \begin{pmatrix} x_1 \\ x_2 \\ \vdots \\ x_N \end{pmatrix}, \ddot{\mathbf{x}} = \begin{pmatrix} \ddot{x}_1 \\ \ddot{x}_2 \\ \vdots \\ \ddot{x}_N \end{pmatrix} \quad (9)$$

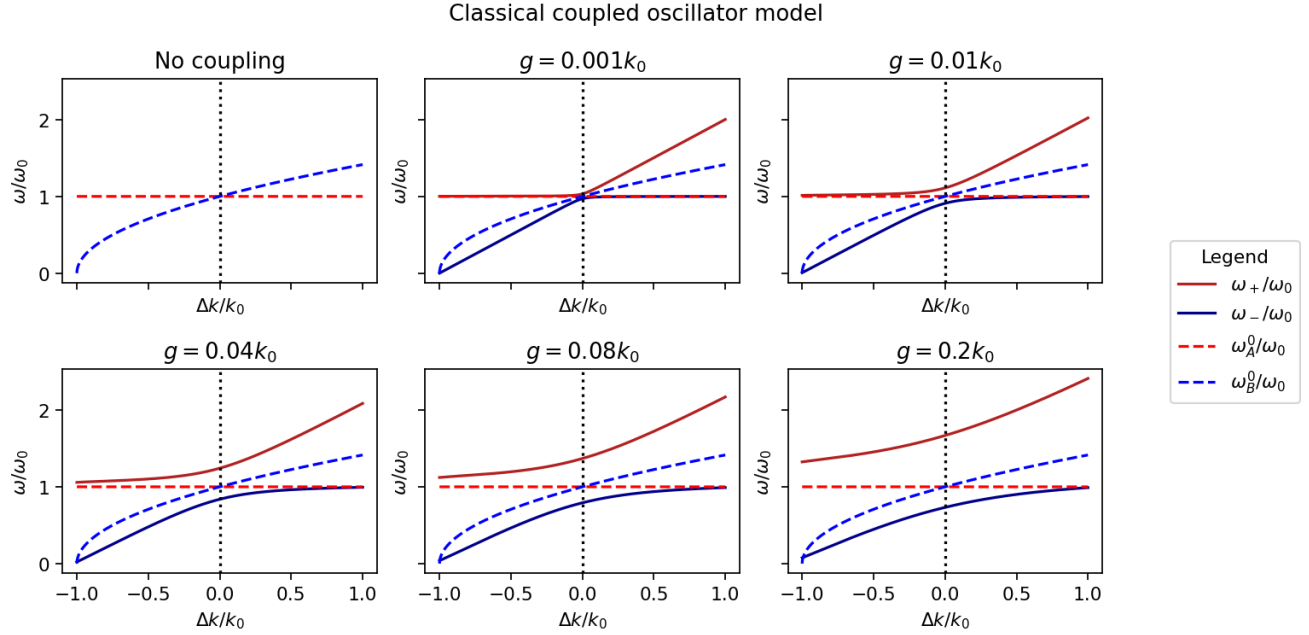


Figure 2: Eigenfrequencies for the classical coupled oscillators A and B which when uncoupled oscillate at $\omega_{A,B}^0$, of equal mass and with spring constants k and $k + \Delta k$, at various coupling strengths g .

This differential equation has normal modes in the form $\mathbf{x} = \mathbf{A}e^{i\omega t}$, such that \mathbf{A} are the eigenvectors of the system, and ω are the eigenfrequencies of the system satisfying (10) [38].

$$\mathbf{M}^{-1}\mathbf{K}\mathbf{A} = \omega^2\mathbf{A} \quad (10)$$

In the case of damped oscillators, we can include a dampening term for each oscillator, $-\Gamma_i\dot{x}$ in our equation of motion. We can thus define $\mathbf{\Gamma}$ as a diagonal matrix containing only $-i\Gamma_i$ terms. This change makes the eigenfrequencies complex, where a negative imaginary component represents a mode that decays over time as a result of incorporating our linewidths [35] [39]. This thus changes (10) into (11).

$$\mathbf{M}^{-1}\mathbf{K}\mathbf{A} = \omega^2\mathbf{A} - i\omega\mathbf{\Gamma}\mathbf{A} \quad (11)$$

Therefore, the characteristic matrix for the coupled oscillator model for N oscillators employed in this project is given by (12), using energy instead of frequency to create a Hamiltonian matrix:

$$\mathbf{H} = \begin{pmatrix} E_1 - i\Gamma_1 & K_{1,2} & \dots & K_{1,N} \\ K_{2,1} & E_2 - i\Gamma_2 & \dots & K_{2,N} \\ \vdots & \vdots & \ddots & \vdots \\ K_{N,1} & K_{N,2} & \dots & E_N - i\Gamma_N \end{pmatrix} \quad (12)$$

The present model was based on code provided by Dr Hamid Ohadi created for [3]. The starter code was written in Mathematica, and was only for the single exciton coupled to cavity photon case. Thus for this project the code was translated to Python and expanded to handle multiple excitons. From this model, the eigenvalues determine the allowed eigenenergies and linewidths of our system, and the eigenvectors determine the Hopfield coefficients [40]. These coefficients, introduced by Hopfield in 1955, describe the relative contributions of the exciton and cavity photon to the created polariton [41, 42].

2.2 Coupled oscillator Model

2.2.1 Polariton case

Single exciton:

First, we begin by considering the case of a single exciton coupled to the cavity photon. If we model only one coupled longitudinal mode, the cavity energy dispersion is quadratic and follows [3]:

$$E \approx \hbar\omega_c + \hbar^2/k_{\parallel}2m_{cav} \quad (13)$$

Where ω_c is the resonant frequency that produces the longitudinal confinement, and m_{cav} is the effective mass of the light in the cavity. Over the relevant in-plane momenta, the much larger effective

mass of the excitons means that their dispersion is essentially flat [3].

For this case, we can create a 2×2 Hamiltonian matrix where the diagonals represent the cavity and exciton respectively, and the off diagonals contain the coupling constant g following a model originally created by Dr Hamid Ohadi. For both the cavity and the exciton there is an associated linewidth Γ that represents the dampening of that particular oscillator. Thus, we can include the dampening as the imaginary part of our Hamiltonian matrix and the energy as the real part as such:

$$\begin{pmatrix} E_{cav} - i\Gamma_c & g \\ g & E_{exc} - i\Gamma_{exc} \end{pmatrix} \quad (14)$$

As this is a Hamiltonian, its real eigenvalues are the eigenenergies of the two possible polaritons. Plotting the eigenenergies of this Hamiltonian reproduces Fig 2 with one uncoupled frequency as a flat line and the other as a quadratic function.

Multiple excitons:

The model is built on the excitonic energies, excitonic linewidths, and oscillator strengths determined from the empirical data, along with the cavity linewidth from the TMM. From this data we construct the following Hamiltonian for our system as (15).

$$\begin{bmatrix} E_{cav}-i\Gamma_c & g_1 & g_2 & \cdots & g_{11} \\ g_1 & E_1-i\Gamma_1 & 0 & \cdots & 0 \\ g_2 & 0 & E_2-i\Gamma_2 & \cdots & 0 \\ \vdots & \vdots & \vdots & \ddots & \vdots \\ g_{11} & 0 & 0 & \cdots & E_{11}-i\Gamma_{11} \end{bmatrix} \quad (15)$$

Where the g factors are the oscillator strengths scaled by some common factor and Γ are the linewidths of each component. The reason there is only 1 row and 1 column with coupling factors is because the excitons are coupled to the cavity and not each other. This lack of coupling arises mainly because of the low density of excitons created in the Cu_2O limits the exciton-exciton interactions [43]. The high detuning between the formed excitons also greatly limits their interaction [44]. These dipole-dipole interactions could happen between excitons [43] along with possible diexciton formation between excitons in the same state if there was a higher density [45]. Instead, this low density allows us to stay squarely in the linear optics regime, allowing us to set all other coupling terms to zero.

The real eigenvalues of this matrix thus represent the energy of the 12 possible polaritons created by the coupling. This matches with the results for the classical coupled oscillator as initially coupling one exciton to the cavity produces an upper and a lower polariton, with each subsequent exciton adding another degree of freedom.

A quantum mechanical derivation can be found in [28] where the Hamiltonian of a polariton is given by three sums, the first two representing the Hamiltonians of the non-interacting components, and the third employing the annihilation and creation operators for the photon and quasiparticle. Diagonalizing this Hamiltonian, and solving for the eigenenergies of the system yields the same results as for the coupled oscillator model employed in this project.

2.3 Transfer Matrix Method

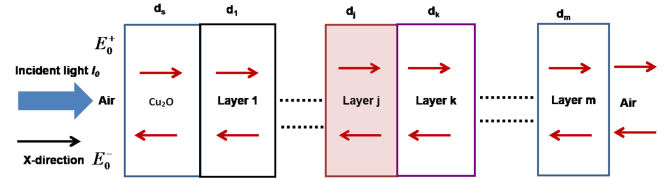


Figure 3: Schema of a DBR for modelling with the transfer matrix method. Each interface between layers as well as propagation through the layer is represented by its own characteristic matrix. Adapted from [46].

The Transfer Matrix Method (TMM) is a mathematical formalism useful for determining the transmission and reflection of a plane wave as it passes through optical materials [47], such as the DBR schema shown in Fig 3. The present model considers varying cavity thickness, the incoming photon wavelength, the angle of incidence, and the refractive index of the optical material used. Ultimately, the transmission and reflection for the optical system was calculated for each configuration. For this model we limit ourselves to the case of linear optics. The model is based on code provided by Dr Sai Rajendran created for [3], translated from Matlab to Python, with some changes and additions made.

Generally, each element or interface of our optical system is represented by a 2×2 matrix. The matrices can relate the electric (or magnetic) vector before the an interface $\begin{pmatrix} E_a^+ \\ E_a^- \end{pmatrix}$ to the vector after the

interface $\begin{pmatrix} E_b^+ \\ E_b^- \end{pmatrix}$, where the $+$ and $-$ signs represent propagation towards or away from the element. At an interface between two materials, these vectors are related via 16 [48].

$$\begin{pmatrix} E_b^+ \\ E_b^- \end{pmatrix} = \mathbf{I}_{a,b} \begin{pmatrix} E_a^+ \\ E_a^- \end{pmatrix} \quad (16)$$

$$\mathbf{I}_{a,b} = \frac{1}{t_{a,b}} \begin{pmatrix} 1 & r_{a,b} \\ r_{a,b} & 1 \end{pmatrix}$$

Where $\mathbf{I}_{a,b}$ is the transfer matrix representing propagation from medium a to medium b, $t_{a,b} = \frac{E_b^+}{E_a^+}$ and $r_{a,b} = \frac{E_b^-}{E_a^+}$. These are the Fresnel transmission and reflection coefficients, and that their value represents the fraction that is transmitted and reflected at a given boundary [49]. These coefficients are thus also subject to Fresnel's equations and Snell's Law relating to optical interface crossing such that θ_i is the angle of incidence and θ_j is the angle the transmitted ray makes to the normal of the interface [49] (19).

The present model considers two possible scenarios: the TM (Transverse Magnetic) polarization or the TE (Transverse Electric) polarization case. The TM case refers to when the magnetic vector of the incident wave is parallel to the boundary plane, whilst TE is the converse electric vector case [49]. If we employ the notation from [49] we can define E as the amplitude of the incident electric vector, E' as the amplitude of the reflected electric vector, and E'' as the amplitude of the transmitted electric vector (H, H', H'' for the magnetic case). Boundary conditions derived from the Maxwell relations, apply differently in the two cases as the tangential component of either the electric or magnetic field must be continuous at the boundary [49]. Thus, for TE: $E + E' = E''$ and for TM: $H - H' = H''$ [49]. Solving the Maxwell equations at the boundary as a system of equations therefore yield two sets of equations for t and r [50].

For the TE case:

$$t_{a,b} = \frac{2n_i \cos \theta_i}{n_i \cos \theta_i - n_j \cos \theta_j} \quad (17a)$$

$$r_{a,b} = \frac{n_i \cos \theta_i - n_j \cos \theta_j}{n_i \cos \theta_i + n_j \cos \theta_j} \quad (17b)$$

For the TM case:

$$t_{a,b} = \frac{2n_i \cos \theta_i}{n_i \cos \theta_j - n_j \cos \theta_i} \quad (18a)$$

$$r_{a,b} = \frac{n_j \cos \theta_i - n_i \cos \theta_j}{n_j \cos \theta_i + n_i \cos \theta_j} \quad (18b)$$

In both cases, the angles and refractive indices are subject to Snell's Law such that:

$$n = \frac{n_2}{n_1} = \frac{\sin \theta_i}{\sin \theta_j} \quad (19)$$

For propagation through a medium, the phase of the field is what changes [48]. Thus we can relate the electric field before passing through the medium $\begin{pmatrix} E_a^+ \\ E_a^- \end{pmatrix}$ to the vectors after the interface $\begin{pmatrix} E_{a^*}^+ \\ E_{a^*}^- \end{pmatrix}$.

$$\begin{pmatrix} E_{a^*}^+ \\ E_{a^*}^- \end{pmatrix} = \mathbf{P}_a \begin{pmatrix} E_a^+ \\ E_a^- \end{pmatrix} \quad (20)$$

$$\mathbf{P}_a = \begin{pmatrix} e^{i\delta_j} & 0 \\ 0 & e^{-i\delta_j} \end{pmatrix}$$

Where the propagation matrix \mathbf{P}_a is defined in terms of the phase shift due to the wave passing through the medium δ_j . The phase shift depends on the wavelength of the light passing through λ_0 , and the complex refractive index of the material \tilde{n}_j , the thickness of the material d_j and the angle at which it enters θ_j . The real part of the refractive index thus applies the phase shift whilst the imaginary part represents attenuation or gain in transmission depending on if it is positive or negative respectively [51]. The phase shift of a ray propagating at an angle through a medium of constant refractive index is equal to the path difference of the ray compared to travelling in a vacuum, divided by the effective wavelength in the medium (21) [52].

$$\delta_j = 2\pi \tilde{n}_j d_j \cos \theta_j / \lambda_0 \quad (21)$$

One key application for TMM calculations is to model complex optical systems like those constituting the DBRs used in [3]. A DBR is made from stacking high and low refractive index optical materials in a layered structure, each layer partially reflecting the light and all the partial reflections ultimately adding up to a very strong total reflection [53]. Ideally, each layer is $\frac{\lambda_c}{4n}$ thick, where λ_c is the central wavelength for which one wants to optimize reflection and n is the refractive index of the layer in question [54]. In this configuration, the effective

wavelength would get modulated to $n\lambda_c$ whilst inside the medium [49]. This value means that the path difference between a ray reflected on the entry to the medium, and one reflected on exiting the medium will thus be $\frac{n\lambda_c}{2n}$, which is equivalent to a phase shift of π , or the condition for destructive interference. The interference shifts to constructive when one considers how DBRs are designed. At exactly one of the boundaries the light must be going from a lower refractive index to a higher one, giving it an additional shift of π , ensuring an overall 2π phase difference between the rays, constituting constructive interference [53].

Using the results from (16) and (20) we can generate the characteristic matrix of DBRs. Each interface and thin film gets its own characteristic 2×2 matrix. These are multiplied by each other in the order that light would pass through them in the cavity. We can start with the 2×2 identity matrix, and perform the matrix multiplication representing the transition from air to the first DBR medium. This matrix can then be multiplied by the propagation matrix for the medium in question, before reaching another interface and the process repeats again. Finally, one can perform an exiting transmission from the last layer again reaching air. The resultant matrix from these calculations is the characteristic matrix for the optical system (22) [48].

$$M_{DBR} = I_{N,\text{air}} \times P_N \times I_{N-1,N} \times P_{N-1} \times \dots \times I_{1,2} \times P_1 \times I_{\text{air},1} \times \mathbf{I}_{2 \times 2} \quad (22)$$

Here, one is considering a DBR of N layers surrounded by air. (22) can also be extended to model a cavity surrounded by DBRs on either side by considering N layers above, M layers below, and a cavity with a propagation matrix over a large distance with refractive index ≈ 1 .

The reflection and transmission for the overall system will therefore be given by Eq 23.

$$t = \frac{E_N^+}{E_0^+} = \frac{1}{(M_{DBR})_{1,1}} \quad (23a)$$

$$r = \frac{E_0^-}{E_0^+} = \frac{(M_{DBR})_{2,1}}{(M_{DBR})_{1,1}} \quad (23b)$$

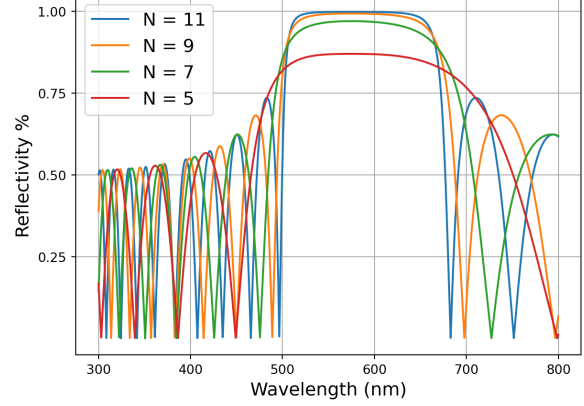


Figure 4: Reflectivity for various numbers N of DBR layers, calculated via the TMM method. Modelled after code from [55].

3 Data Extraction

3.1 The phonon background

The yellow Rydberg exciton series observed in [3] sits atop a phonon-assisted absorption into the excitonic ground state [56]. Phonons are quasiparticles denoting vibrational normal modes in the lattice structure of the Cu_2O crystal [57]. The phonons represent quanta of the ions in the lattice's displacement fields [58]. This assistance interacts with the excitonic absorption peaks (24), giving them a characteristic Fano absorption profile [56].

$$\alpha_n \propto \frac{\frac{\Gamma_n}{2} + 2Q_n\Delta_n}{\left(\frac{\Gamma_n}{2}\right)^2 + \Delta_n^2} \quad (24)$$

Where Q_n is an asymmetry parameter, Γ_n is the absorption peak's linewidth, and $\Delta_n = \omega_n - E_n/\hbar$ is the detuning between the energy of the peak and of the laser [3].

The background itself follows a positive square root dependence consisting in the relevant range of three components plus an offset (25) [56]. Each component starts at an excitonic peak offset to the right by the energy of the particular phonon responsible for the assistance [23]. This offset is the product of previous square root terms sufficiently far away from the studied energy range to tend towards a constant value. To be able to analyze the excitonic peaks properly, this phonon background (25) was subtracted from the absorption data from [3].

$$\alpha_p = h_0 + \sum_{i=1}^3 a_i \sqrt{E - E_{\text{peak}_i} - E_{\text{phonon}_i}} \quad (25)$$

After the excitonic peaks there is another component to the phonon background called the Urbach tail [23]. This tail occurs when the exponential growth of the phonon background smoothly transitions into a continuum. Since this occurs after the peaks, this region is not of interest to the model proposed in this paper and as such it is not accounted for.

3.2 Fitting the experimental results

For this project, a different approach was employed compared to other analyses like [5]. In [5] the phonon background was subtracted as a straight line between each of the valleys in the absorption coefficient data. For this project, a master fitting function was employed, simultaneously fitting 12 Fano peaks alongside 3 phonon backgrounds and a constant offset. This project is the first of its kind to have fitted the peaks simultaneously with the phonon background, with one overall fit covering almost all datapoints.

Initially a recursive approach was used where the first peak was fitted by itself using a Fano absorption profile added together with a square root dependent phonon absorption profile. The parameters from this fit were then used to perform the same fit on the next peak, and so on, until all the peaks were fitted. This approach thus produces a decent fit of the Fano absorptions, but it does not represent the phonon background correctly as it includes 11 phonon background components, whereas we know there are three dominating terms.

The parameters for this fit were then used as the parameter guesses for a subsequent master fitting function. This function attempts to curve fit 11 Fano profiles added to 3 phonon backgrounds plus one initial offset. This process is similar to performing an Elliot fit as derived in [59], where one fitting component is simply the peak and the second is the continual rise in value [28, 60]. The function starts off the phonon absorption profiles at 2.115 eV, the first local minima of the dataset, and the third local minima in accordance with the phonon background for Cu_2O as described in [23]. The function man-

ages to fit all the data up to the last 3 peaks with high accuracy (Fig 5).

The reason for the divergence at the last 3 peaks is probably due to the low number of datapoints constituting those peaks and the large number of fitting parameters. Generally, computational fitting functions cannot fit a function with N parameters without having at least N datapoints. In the present case, the master fitting function uses 48 parameters, where 4 parameters are specific to each Fano absorption peak. Thus, when the last 3 peaks have 6, 6, and 4 constituent datapoints respectively, it could explain why the curve fitting diverges for these peaks. Computational limitations for this project, and the limited time available to let calculations run, could also be the explanation.

For the last three peaks, it is possible to identify which datapoint closest approximates the peak, and the distance between which two datapoints best represents the width of the peak. With these parameters determined manually, they were held constant and the last three peaks were fit (Fig 6).

3.3 Data analysis

As discussed in [4], the energy of the excitons should follow the Rydberg formula for high n as these behave approximately like Rydberg atoms. As can be seen in Fig 7A, the energies are fitted very well by (1). By curve fitting the peak energies to the Rydberg formula we obtain a band gap energy $E_g = (2.172569 \pm 9 * 10^{-6}) \text{ eV}$ and a Rydberg energy of $Ry = (0.09758 \pm 1.0 * 10^{-4}) \text{ eV}$ where the uncertainty is determined from the covariance of the curve fit. For the sample used in [4] the values were 2.17208 eV for E_g and $Ry = 92 \text{ meV}$. The difference in the band gap energy can likely be explained by the temperature difference between the samples, with the sample from [3] being at 4K whilst the sample from [4] was at 1.2K. Indeed, the bandgap of Cu_2O has been shown to increase with temperature [61], as is the case for these results. With regards to the Rydberg constant this value is almost precisely the same 97 meV that [3] assigns Cu_2O .

For a better fit of the peaks accounting for this divergence, quantum defects can be accounted for. These defects can arise from interactions with the surrounding crystal, with phonons, or from non-parabolicity of the effective mass etc. [4, 62]. Accounting for the defects is done by replacing n with

Curve fit and experimental data of absorption spectrum

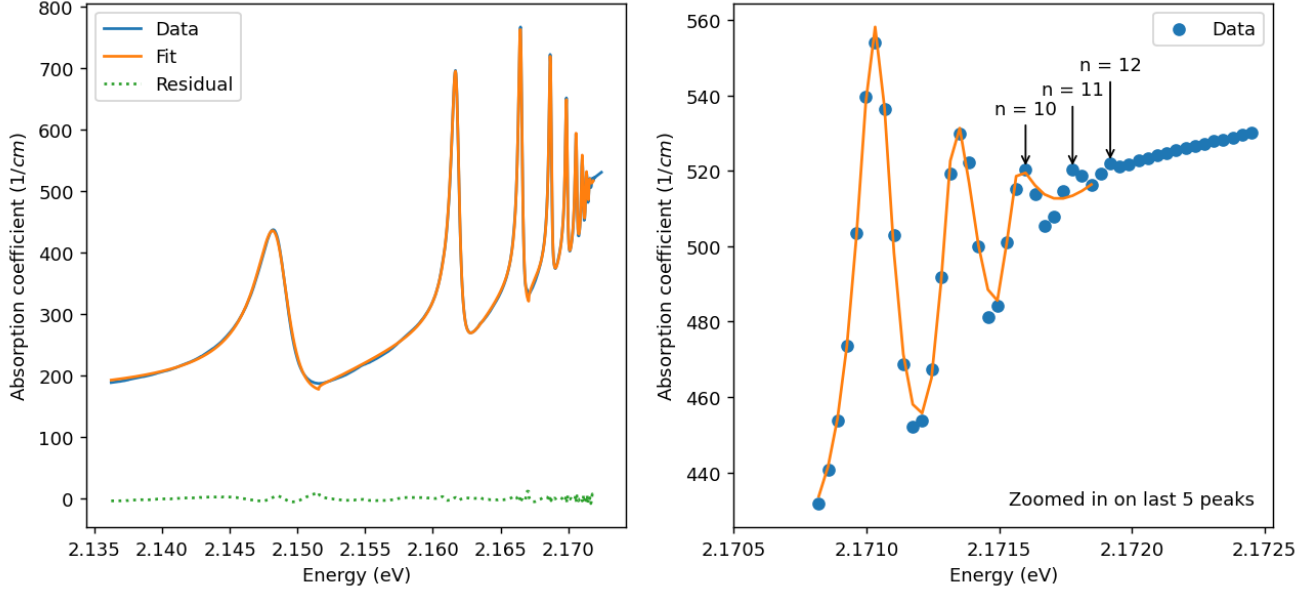


Figure 5: Absorption spectrum for Cu_2O from [3] and curve fit of 12 Fano peaks with 3 phonon backgrounds.

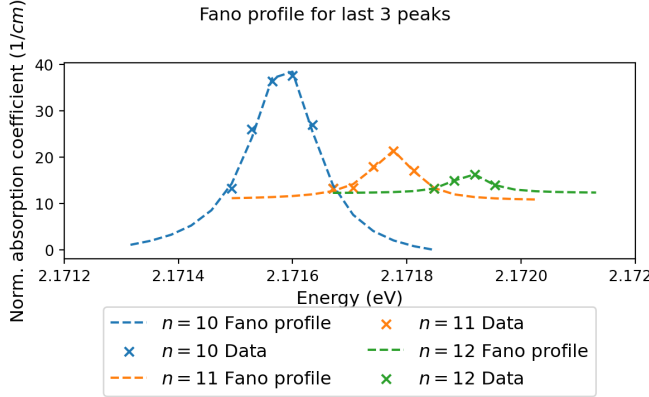


Figure 6: Curve fitted Fano profiles for the last 3 absorption peaks. Shown here with the background subtracted as a straight line between valleys.

$n - \delta_l$ where δ_l is the quantum defect [4]. With this replacement, (1):

$$E_n = E_g - \frac{Ry}{(n - \delta_l)^2} \quad (26)$$

Curve fitting the peak energies to Eq 26 thus yields a much-improved fit, with $\delta_l = 0.099 \pm 0.001$. Using the curve fit of the absorption data from [3], the linewidth and oscillator strength could be determined. The linewidth associated with each peak was a fitting factor in the curve fitting function for all but the last three peaks. For the last three peaks

the linewidth was determined differently. The first two widths are the fitting parameters determined for the partially manual fit, and the last width is estimated entirely manually since the peak in total only consists of 3 datapoints.

In accordance with the results from [4] a deviation can be seen in the linewidths for higher n values, which coincides with the excitonic peaks getting more and more Gaussian in shape. The change in shape is likely due to the shorter linewidths of later peaks entailing less of an asymmetric Fano assisted profile, due to the limited change in phonon background over such a short range [4]. The deviation is likely due to the larger principal quantum number excitons having a larger extension and therefore experiencing more of the crystal inhomogeneity [4]. For the oscillator strengths the divergence from the theoretical results could be caused by blockade effects between excitons. These arise from the increased energy required to excite subsequent excitons due to the dipole interaction energy of the already present excitons [4].

The relative oscillator strengths were determined from integrating the absorption spectrum from valley to valley. The respective proportionality of these strengths is accurate, since it is precisely the coupling alone that is capable of generating such peaks [4]. However, the size of these strengths needs to

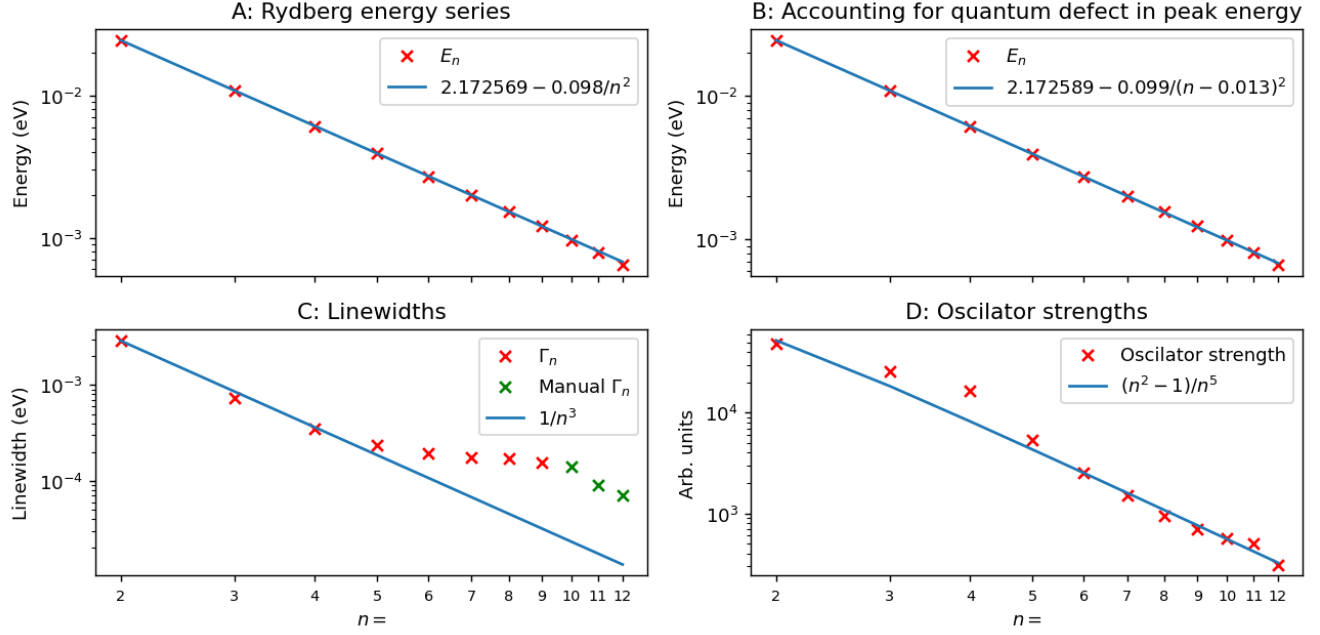


Figure 7: Fitted parameters and their theoretical predictions over principal quantum number n from the curve fit of the experimental data. Peak energies compared with A: Rydberg series (1), B: quantum defect fit (26). C: Linewidths from Fano fits (24) where last 3 are from the partially manual fit in Fig 6, D: Oscillator strength from integrating absorption data without phonon background.

be scaled to accurately represent the dimensionless oscillator strength. In quantum mechanics, this quantity represents the transition matrix element squared, multiplied by some constants representing the type of coupling [28].

The oscillator strength f is related to the dielectric function $\epsilon(\omega)$ through (27)

$$\epsilon(\omega) = \tilde{n}_{bg}(\omega) + f \frac{\Gamma_n/2 + 2Q_n\Delta_n}{(\Gamma_n/2)^2 + \Delta_n^2} \quad (27)$$

Where \tilde{n}_{bg} is the complex refractive index of the material the coupling is taking place in [28], the other terms are as defined in (24). $\epsilon(\omega)$ can also be related to the complex refractive index, generally as $\sqrt{\epsilon(\omega)} = \tilde{n}(\omega)$.

Therefore, to attain a scaling for our oscillator strengths, we take the difference in refractive index of Cu_2O between the second peak and the first valley, and square it to get a value for $\Delta\epsilon$ associated with that absorption peak. The second peak is chosen due to its good curve fit, and strong coupling. This $\Delta\epsilon$ can then be inserted into (27) at zero detuning, alongside the refractive index at the valley for \tilde{n}_{bg} . Finally, to get a scaling constant, we relate the value of f to the oscillator strength previously determined for this peak, finding the necessary scal-

ing to be around one part in 23 million. It is thus the integrated areas, multiplied by this scaling that serves as the coupling constants in the coupled oscillator model in later sections.

4 Modelling results

4.1 TMM calculations

The TMM model for this project generates the characteristic matrix from (22) and uses it for 13 and 10 layers of SiO_2 and Ta_2O_5 with experimental data for the refractive index for these and Cu_2O at different wavelengths provided by Dr Sai Rajendran for usage in [3].

Holding either the angle or thickness of the cavity constant and varying the other thus allows excitons to be identified as gaps in the transmission of the sample at specific energies, corresponding to the excitonic resonances seen in the experimental transmission data (Figure 8) [3].

In the lower panel of Fig 8, vacuum Rabi Splitting (VRS) can also be identified by the asymmetry of the transmission near the excitonic resonances [10], showing one peak before and one after the excitonic resonance with a splitting in between. The VRS is

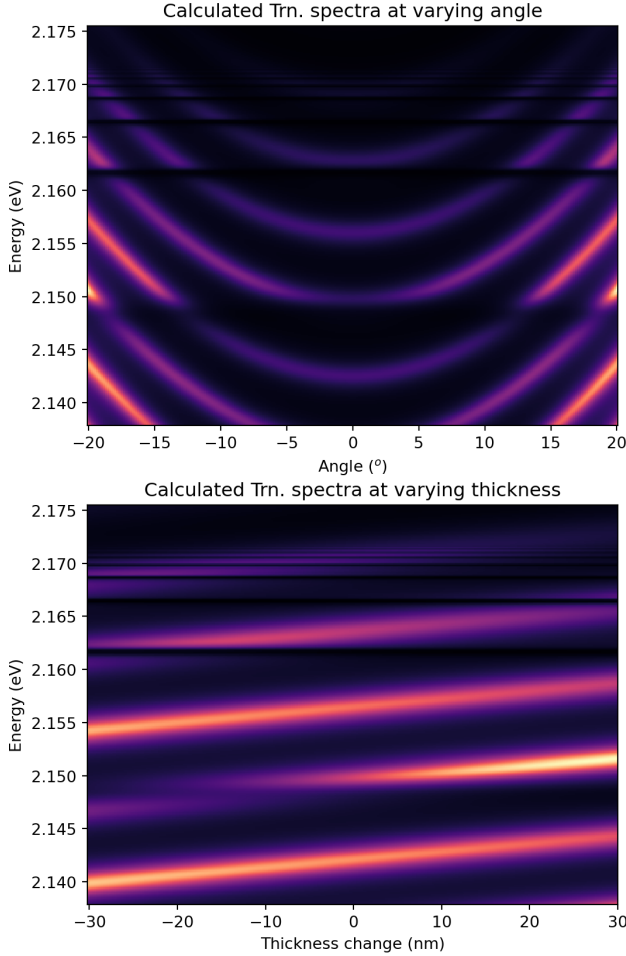


Figure 8: Results of TMM calculations showing absorption characteristic of excitons and polaritons. (Upper - Momentum-space spectra for variable angle, Lower - real-space spectra for varying cavity thickness)

a clear indication of the strong coupling regime, as it indicates that the exciton-polariton has two new eigenenergies.

The transfer matrix method calculations can also be used to find the linewidth of the cavity. This linewidth corresponds to the decay rate of the cavity construed as an oscillator, arising from the losses to the mirrors. We can find the linewidth by setting the refractive index of the Cu_2O sample to $1 + 0i$, modelling a cavity filled only with vacuum. From this, the cross-section of the cavity transmission spectra was taken and the FWHM was calculated. Thus, we can determine that $\Gamma_c = 7.419 \times 10^{-5}$ which will be used for the coupled oscillator model.

4.2 Coupled oscillator model calculations

4.2.1 Energy eigenvalues

The energy eigenvalues for the coupled oscillator model using experimental data can be seen in Fig 9. From the left panel it is clear that due to the limited strength of the coupling modelled, the avoided crossings are not visible unless one zooms in on either of the regions of zero detuning. This is to be expected since the energy splittings generated by this size of linewidths and coupling strength is much too small for the scale of the left panel (Fig 10).

In the right panel, the energies of the 12 possible polaritons can be seen. At each point of zero detuning between an exciton energy and the cavity energy a distinct upper and lower polariton can be seen. These areas around the points of zero detuning strongly resemble the classical model shown in Fig 2. As will be discussed, this is a result of the Hopfield coefficients for two polaritons dominating at these points, making the model resemble the 2×2 case.

4.2.2 Splittings and Hopfield Coefficients

As we can see in Fig 9, barring the first and last polariton, the shape of each polariton is such that they first act as an upper polariton in relation to the one before them, then as a lower polariton to the one following them. The result of this is that we can organize the polaritons into 11 upper-lower pairs similar to the classical case from which 11 splitting energies can be determined. As discussed, the values of these splittings allows us to investigate the

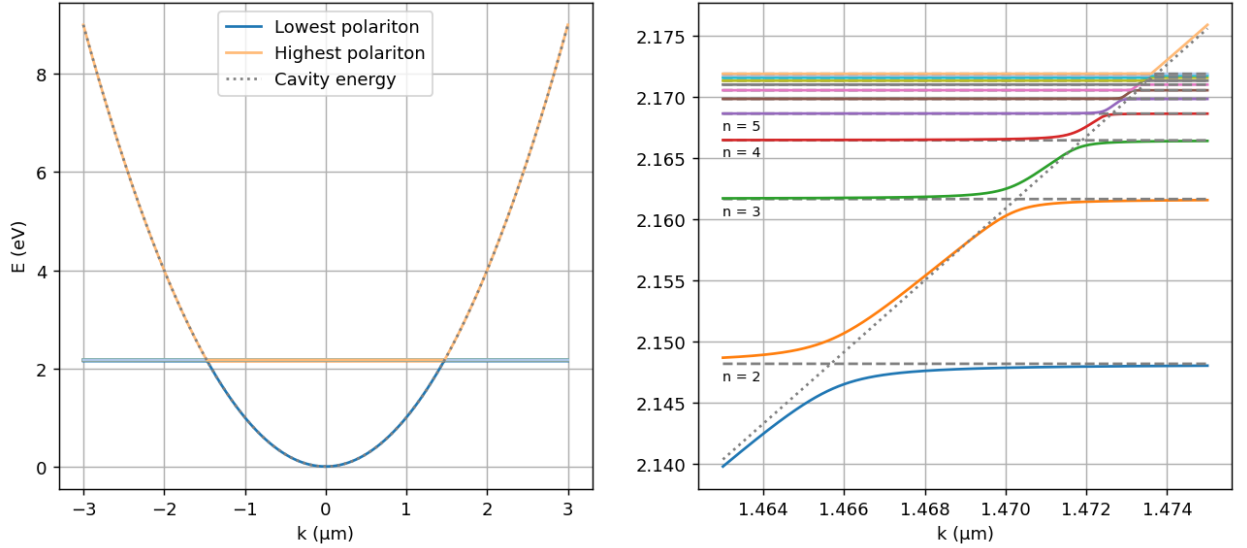


Figure 9: Eigenenergies of the coupled oscillator model for 11 excitons coupled to a cavity photon. The right panel is zoomed in on positive points of zero detuning, with exciton energies given by horizontal dashed lines.

coupling strength of each exciton to the cavity.

If we plot the value of these splittings alongside our oscillator strengths normalized such that the first element of each is the same, we get a perfect match. This is not surprising as it is precisely these coupling factors that create this splitting. Nevertheless, this is a good indication that the model is faithfully coupling all 11 excitons to the cavity photon (Fig 10).

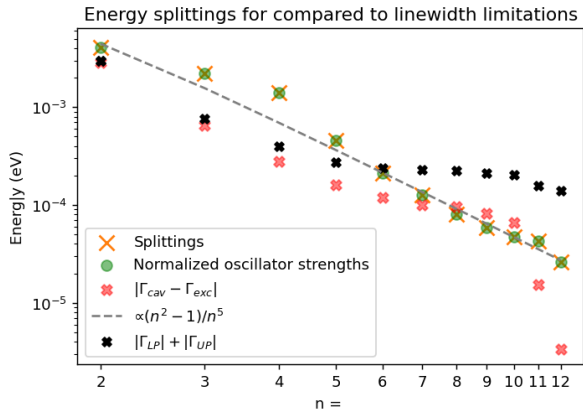


Figure 10: Energy splittings and normalized oscillator strengths for each of the 11 polariton splittings. Also plotted are limitations for strong coupling outlined in (30) and (33), where Γ denotes the linewidth for the cavity, exciton, upper, or lower polariton for a given principal quantum number n .

As the polariton is a part light, part matter quasi-particle we use Hopfield coefficients to quantify the probability of measuring it as an exciton or a photon [63]. These coefficients are thus a function of the in-plane momentum k_{\parallel} , and since they are probabilities they are subject to the condition that their absolute value squared must always add to 1. For the simplest case of one exciton coupled to the cavity photon, we expect the cavity to dominate for all momentums far from the excitonic resonance, and for the exciton to dominate in the region between the points of zero detuning. For this case the Hopfield coefficients are simply the absolute value squared of the components of the first eigenvector of the Hamiltonian. The second eigenvector can be used as well, with the components just switching places. This can be seen below (11) where the Hopfield coefficients always sum squared to one, and at the points of zero detuning where the exciton and cavity energies are equal, there is an equal probability of either.

For the case of multiple excitons the Hopfield coefficients behave slightly differently. For large absolute values of k_{\parallel} the cavity dominates as before, and between the points of zero detuning the lowest polariton dominates. As one approaches the point of zero detuning, each n^{th} excitonic resonance energy is reached in turn, causing the Hopfield coefficient

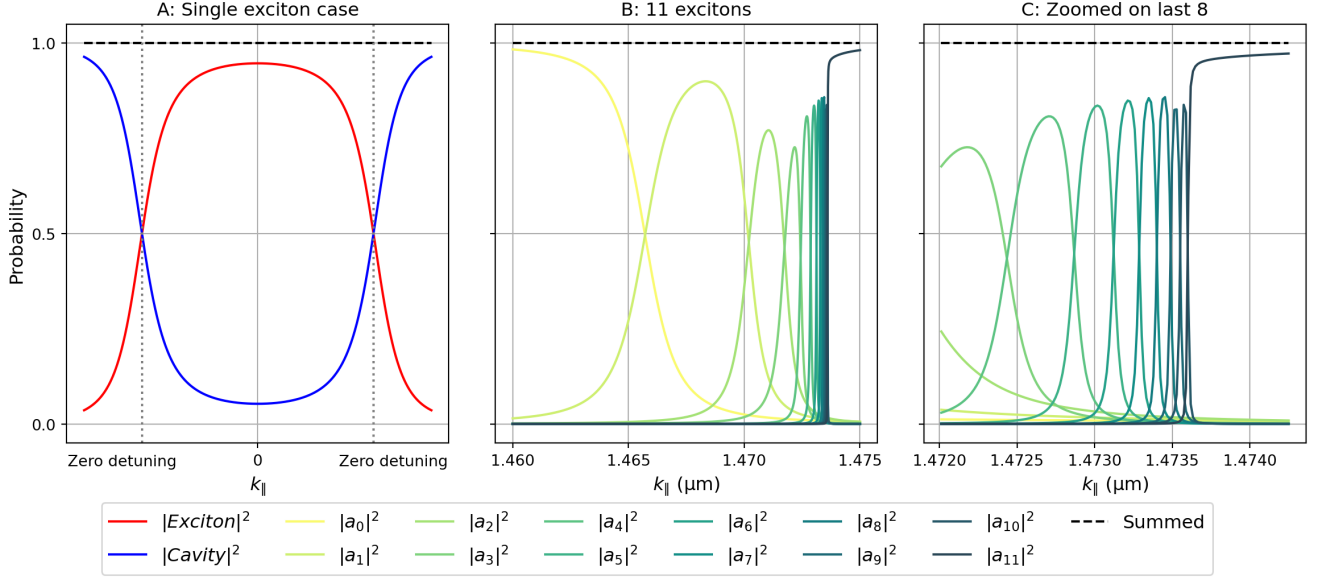


Figure 11: Hopfield coefficients for A: a general single exciton coupled to a cavity, B: the 11 excitons coupled to a cavity photon using experimental data, C: zoomed in on end. $|a_n|^2$ represents the coefficient for the n^{th} energy mode such that $|a_{11}|^2$ is the cavity and the rest are excitons of increasing energies.

corresponding to the n^{th} polariton to rise up and dominate before subsiding, giving way to the next polariton's resonance. The resonances of the polaritons bleed into one another as well, such that at the point where one dominates, others still capture a significant percentage, as seen by the discrepancy between resonant peaks and the sum of all coefficients.

4.2.3 Intensity plots

With the eigenenergies and the Hopfield coefficients from the eigenvectors, intensity plots can be generated for the polaritons. If one considers a range of energies and momenta the intensity plots show the shape of each polariton, modulated by its Hopfield coefficients along the k axis and modulated by its linewidth and energy drop-off along the E axis. The formula for the intensity of the n^{th} polariton is thus given by (28) [64].

$$I(k, E)_n = (f(\vec{k}))_n^2 \frac{Im[\lambda_n]^2}{Im[\lambda_n]^2 + (E - Re[\lambda_n])^2} \quad (28)$$

Where $f(\vec{k})$ is the first eigenvector of the Hamiltonian, meaning that, $(f(\vec{k}))_n^2$ represents the n^{th} coefficient of the vector squared, or the n^{th} Hopfield

coefficient. λ_n represents the n^{th} eigenvalue of the hamiltonian such that the real part is the energy eigenvalues and the imaginary part represents the linewidth of the polariton in question. The intensity is simply the inverse of the polariton absorption which can be derived from the Heisenberg equations of motion as done in [64].

As such (28) shows that the intensity of the polariton will increase as one approaches its eigenenergy, and is overall scaled by the linewidth of the polariton and modulated by the Hopfield coefficient in k space. Summing the contribution for all 12 polaritons allows us to plot the overall intensity (Fig 12 A,B).

The number of polariton splittings for the experimental configuration, 5, is less than the number of excitons used in the model as seen in Fig 12 A. This thus replicates the discrepancy between number of excitons and splittings found in [3], finding polaritons only up to $n = 6$.

Therefore we can investigate the effect of decreasing the linewidths used, or of increasing the coupling strength on the number of splittings (Fig 12 C-F). Modelling with all linewidths decreased by a factor of 10, all 11 splittings become identifiable. For a coupling strength increased by a factor of 3.5, 5 polariton splittings are now discernible.

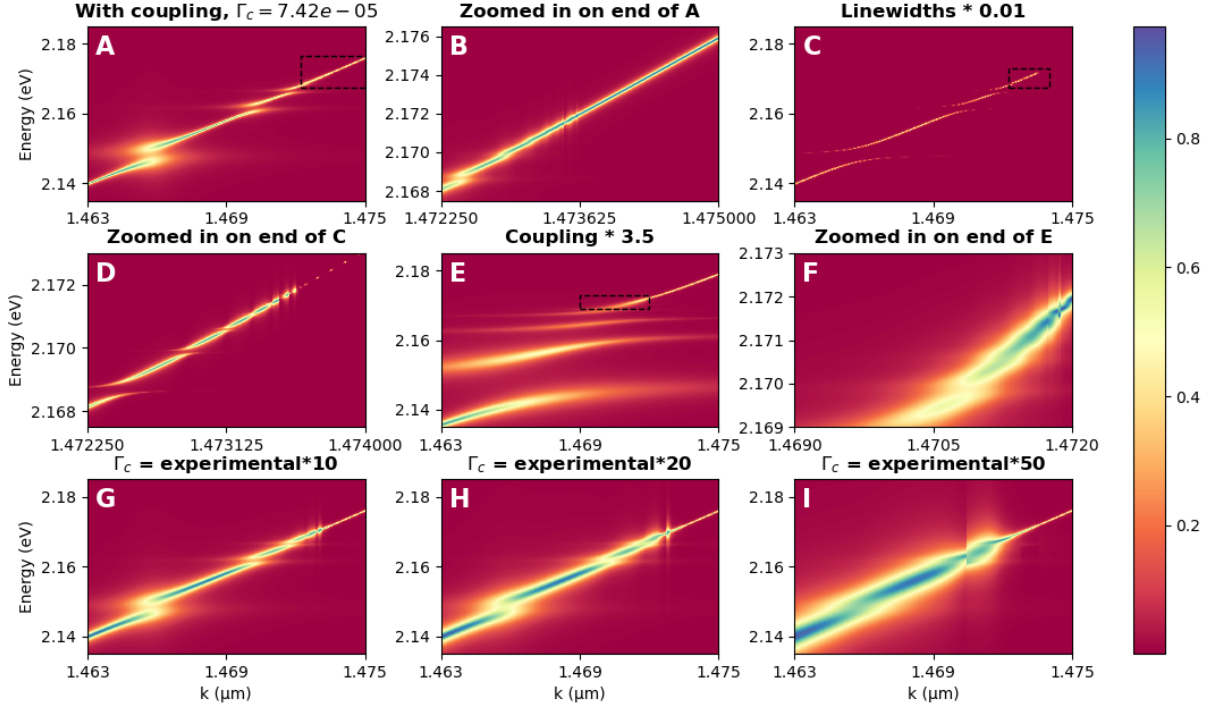


Figure 12: Polariton intensities determined from coupled oscillator model for A,B: experimental parameters, C,D: zero coupling, E,F: decreased linewidths, G,H: increased coupling constants, I-L: different cavity thicknesses. Black boxes denote zoom region for next graph.

Increasing the cavity linewidth will smear out the polaritons, impeding the formation of polariton splittings. Therefore, the anticrossings that can be seen in Fig 12 A, can be absorbed by the cavity linewidth, obstructing the resolution of higher order polaritons (Fig 12 G-I). In Fig 12 G-I we can clearly see that increasing the cavity linewidth renders the anticrossings less and less clear, starting first with the more weakly coupled higher orders, but ultimately encompassing all polariton splittings.

4.2.4 Varying Γ_c

Finally incorporating all aspects of this analysis, we can account for the cavity linewidth changing with energy. This is the result of the phonon absorption background changing with energy as seen in Eq 25. Since this background represents photons absorbed by the Cu_2O that do not become excitons, it can be incorporated into our model as part of the linewidth of the cavity as an imaginary refractive index. The TMM calculations can be run with a cavity of refractive index $3 + ki$ where $k = \lambda\alpha_p/4\pi$ and a_p represents the phonon background. The transmission

spectra for an empty cavity accounting only for the phonon background can be seen in Fig 13 A.

From these calculations we can take the cross-section for the transmission spectra, and plot it for each energy. From here, a FWHM of the cross section can be calculated, associated with each energy. This FWHM is the linewidth of the cavity for a given energy Fig 13 B.

In Fig 13 C, we can see that the linewidth changes with energy along the same shape as the phonon absorption background. This means that we can perform a curve fit of the linewidth to a linear multiple of the absorption background to determine their relation, which was found to be $\Gamma_c = 1.38 \alpha_p$. With this relation for Γ_c , the intensity plots can be calculated again, this time with the energy dependence.

From Fig 13 D, we can see that the modulated Γ_c causes the Vacuum Rabi Splitting to disappear for some of the higher n excitons.

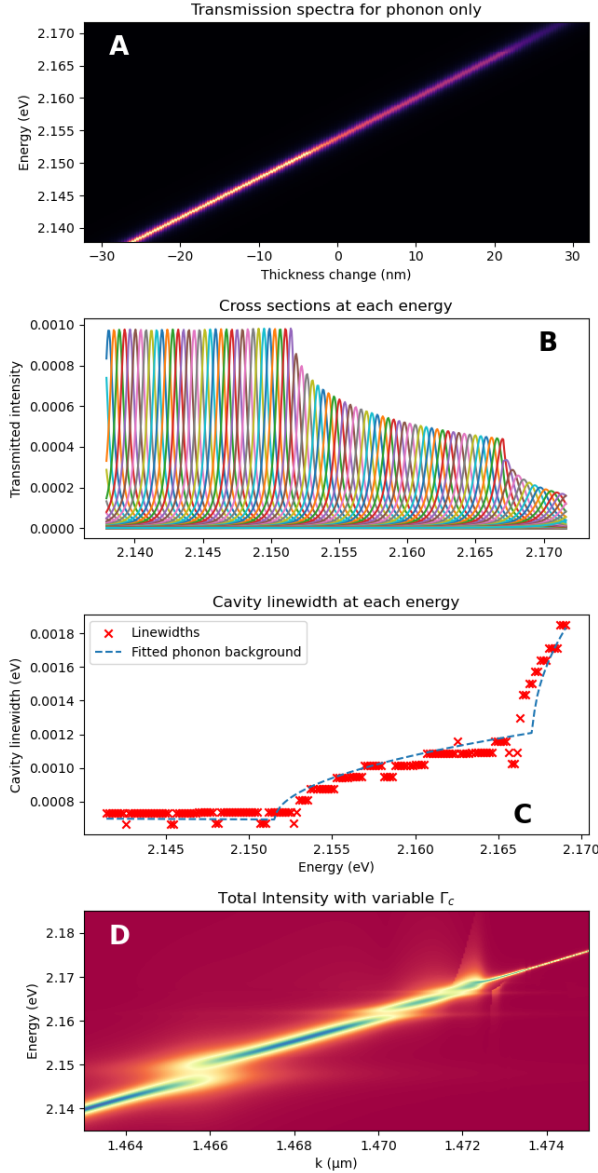


Figure 13: Showing A: The TMM transmission spectra for an empty cavity save for the imaginary component of the refractive index of Cu_2O representing the phonon background. B: The cross section of each datapoint in A. C: The linewidth of each curve in B, alongside a curve fit to (25). D: The intensity plot for the empirical values, given a cavity linewidth that changes with energy as shown in C.

5 Discussion

The equation for the vacuum Rabi splitting is $\hbar\Omega = E_{UP} - E_{LP} = 2g$ [65]. This is theoretically attainable for each exciton, so we can consider the 2×2 Hamiltonian case in isolation, since there is no coupling between the excitons themselves. Taking the eigenvalues of (14) we use the exciton energy E_{exc} and the cavity energy E_{cav} , along with their linewidths to find (31).

$$E_{LP,UP}(k_{\parallel}) = \frac{1}{2}(E_{exc} + E_{cav} - i(\Gamma_{exc} + \Gamma_{cav})) \pm \sqrt{4g^2 + (E_{exc} - E_{cav} - i(\Gamma_{exc} - \Gamma_{cav}))^2} \quad (29)$$

From (31), it can be derived that the weak versus strong coupling regime is differentiated by the square root being imaginary or real respectively [5, 66]. As discussed, the real value contributes a change to the energy of the polariton modes giving rise to VRS. An imaginary value instead contributes towards changing the linewidth of the cavity or exciton mode through a process known as the Purcell effect [67]. At the point of zero detuning when $E_{exc} = E_{cav}$, this enforces the condition of (30).

$$\hbar\Omega = 2g > |\Gamma_{cav} - \Gamma_{exc}| \quad (30)$$

However this condition would entail VRS for immensely large linewidths, given that they were sufficiently close together, which is not observed [68]. Instead, the linewidths of the upper and lower polariton modes quickly render the VRS impossible, as they are simply calculated via: [5, 68].

$$\Gamma_{LP} = |X|^2\Gamma_{exc} + |C|^2\Gamma_{cav} \quad (31)$$

$$\Gamma_{UP} = |C|^2\Gamma_{exc} + |X|^2\Gamma_{cav} \quad (32)$$

Where, X and C are the Hopfield coefficients as shown in Fig 11 A. These linewidths thus impose a second condition of (33) to ensure that the splitting is discernible [5].

$$\hbar\Omega > |\Gamma_{UP}| + |\Gamma_{LP}| \quad (33)$$

From these considerations we can see that it must be the interplay between the experimental linewidths and oscillator strengths that renders higher order polariton splittings impossible.

These conditions (30) and (33) were plotted in Fig 10, and compared to the energy splitting from the model. These results explain the numbers of splittings seen in Fig (28) A,B. First a slightly obscured splitting is seen, followed by 3 clearer splittings, and lastly two slight indications of splitting. This coincides with the datapoints from Fig 10, in that for $n = 2$, the splitting sits about equal to the imposed conditions, whereas for $n = 3, 4, 5$ the splitting is greater than the conditions, creating the clear splittings seen. For $n = 6, 7$ and onwards we can see that the energy splitting fails to meet the conditions to an increasing extent, explaining why clear upper and lower polaritons are not seen for these values of n .

Furthermore, a thicker cavity with more Cu_2O would be able to absorb more light to create excitons, which in turn would increase the area of the excitonic peaks, and thus the coupling strengths [69]. With an increase in coupling strength, higher order polaritons should become discernible (Fig 12 A vs G). However, as we have seen from the TMM calculations, there is an inherent photon loss that comes with the Cu_2O due to the phonon absorption. Thus, a thicker cavity would also lead to a greater cavity linewidth, which as discussed can obscure the presence of polariton splitting.

Lastly, the model supports this discussion showing that with decreased linewidths, polariton splittings can be identified for all n values (12 E, F).

6 Conclusion

Exciton-polaritons at high principal quantum numbers and their applications for quantum technologies have received great interest, just like their counterpart, the Rydberg atoms [70, 4, 11, 12]. Especially enticing, the realization of nonlinear optics from exciton-polaritons could prove a leap towards universal quantum computing [71, 72, 73]. Recent work like [71] has demonstrated that Cu_2O is a suitable platform for quantum polaritonics precisely due to the scaling of nonlinearities with higher n values.

The novel modelling outlined in this report shows some of the difficulties with identifying the strong coupling of excitons to cavity photons for higher principal quantum numbers, even when the excitons are clearly present. The strong coupling condition (that the energy splitting is not obscured by the

linewidths) can easily fail to be satisfied, either by the linewidth of the cavity or excitons, or as a result of too weak coupling.

The modelling presented here demonstrates polariton formation up to the same order as the experimental data [3]. Alongside this an increase or decrease of the number of polariton splittings is found by varying the parameters as expected from the theory [2, 28, 5].

Further, the results of this modelling points to an interesting balance that can be reached with regards to the cavity thickness. In [3], the authors posit that the competing factors of exciton formation and phonon absorption discussed could be used to determine a finite ratio of VRS to polariton linewidth. Future investigations into this using both the TMM model, and the coupled oscillator model discussed in this project could prove fruitful in this regard. Modelling VRS and the linewidth conditions for a range of thicknesses could help identify this ratio, its position, and any variance it may have respective to other variables.

TMM calculations similar to the model presented in this paper also show that without the phonon absorption background, the number of excitons that can be identified equals the number of polaritons [5]. Future models could tune the cavity width to try to optimize for the greatest number of observed splittings. One recent study posits that the phonon interaction can be eliminated altogether through the usage of electromagnetically induced transparency (EIT) [72]. Here as well, the type of modelling considered in this project could be extended to include EIT, such that the disappearance of the phonon background could also be optimized for in the search for higher order polariton splittings.

Ultimately, recent literature indicates that the realization of high-lying polariton states could pave the way for applications within nonlinear optics through exploiting the strong interaction and blockade effects inherent to these quasiparticles [72, 74, 4]. Due to the limitations of analytical solutions, models like the one presented here seem a necessary tool for realizing this technological potential. Models can thus bridge the gap between the theoretical derivations, and the experimental applications, allowing the fine tuning of physical values like thickness, DBR layers, or laser frequency towards ever more polariton splittings.

References

- [1] Keeling, J. & Berloff, N. G. Exciton-polariton condensation. *Contemporary Physics* **52**, 131–151 (2011). URL <https://doi.org/10.1080/00107514.2010.550120>. Publisher: Taylor & Francis eprint: <https://doi.org/10.1080/00107514.2010.550120>.
- [2] Knox, R. S. *Theory of excitons*. Solid state physics (Academic Press, New York, 1963). OCLC: 330436.
- [3] Orfanakis, K. *et al.* Rydberg exciton-polaritons in a Cu₂O microcavity. *Nature Materials* **21**, 767–772 (2022). URL <https://www.nature.com/articles/s41563-022-01230-4>. Number: 7 Publisher: Nature Publishing Group.
- [4] Kazimierczuk, T., Fröhlich, D., Scheel, S., Stolz, H. & Bayer, M. Giant Rydberg excitons in the copper oxide Cu₂O. *Nature* **514**, 343–347 (2014). URL <https://www.nature.com/articles/nature13832>. Number: 7522 Publisher: Nature Publishing Group.
- [5] Orfanakis, K. Pathways towards single-polariton nonlinearity: from ground state exciton-polariton condensates in GaAs to Rydberg exciton-polaritons in CuO (2023).
- [6] Kasprzak, J. *et al.* Bose-Einstein condensation of exciton polaritons. *Nature* **443**, 409–414 (2006). URL <https://www.nature.com/articles/nature05131>. Publisher: Nature Publishing Group.
- [7] Xiong, R. *et al.* Correlated insulator of excitons in WSe₂/WS₂ moiré superlattices. *Science* **380**, 860–864 (2023). URL <https://www.science.org/doi/10.1126/science.add5574>. Publisher: American Association for the Advancement of Science.
- [8] Bauer, B., Sharma, R., Chergui, M. & Oppermann, M. Exciton decay mechanism in DNA single strands: back-electron transfer and ultrafast base motions. *Chemical Science* **13**, 5230–5242. URL <https://www.ncbi.nlm.nih.gov/pmc/articles/PMC9093102/>.
- [9] Dufferwiel, S. *Strongly Confined Exciton-Polaritons in a Tunable Microcavity*. phd, University of Sheffield (2015). URL <https://etheses.whiterose.ac.uk/9132/>.
- [10] Khitrova, G., Gibbs, H. M., Kira, M., Koch, S. W. & Scherer, A. Vacuum Rabi splitting in semiconductors. *Nature Physics* **2**, 81–90 (2006). URL <https://www.nature.com/articles/nphys227>. Number: 2 Publisher: Nature Publishing Group.
- [11] Cuevas, *et al.* First observation of the quantized exciton-polariton field and effect of interactions on a single polariton. *Science Advances* **4**, eaao6814 (2018). URL <https://www.science.org/doi/10.1126/sciadv.aao6814>. Publisher: American Association for the Advancement of Science.
- [12] Hertzog, M., Wang, M., Mony, J. & Börjesson, K. Strong light-matter interactions: a new direction within chemistry. *Chemical Society Reviews* **48**, 937–961 (2019). URL <https://pubs.rsc.org/en/content/articlelanding/2019/cs/c8cs00193f>. Publisher: The Royal Society of Chemistry.
- [13] Amo, A. *et al.* Superfluidity of polaritons in semiconductor microcavities. *Nature Physics* **5**, 805–810 (2009). URL <https://www.nature.com/articles/nphys1364>. Publisher: Nature Publishing Group.
- [14] Lerario, G. *et al.* Room-temperature superfluidity in a polariton condensate. *Nature Physics* **13**, 837–841 (2017). URL <https://www.nature.com/articles/nphys4147>. Publisher: Nature Publishing Group.
- [15] Nardin, G. *et al.* Hydrodynamic nucleation of quantized vortex pairs in a polariton quantum fluid. *Nature Physics* **7**, 635–641 (2011). URL <https://www.nature.com/articles/nphys1959>. Publisher: Nature Publishing Group.
- [16] Sanvitto, D. *et al.* All-optical control of the quantum flow of a polariton condensate. *Nature Photonics* **5**, 610–614 (2011). URL <https://www.nature.com/articles/nphoton.2011.211>. Publisher: Nature Publishing Group.

- [17] Opala, A. & Matuszewski, M. Harnessing exciton-polaritons for digital computing, neuromorphic computing, and optimization [Invited]. *Optical Materials Express* **13**, 2674–2689 (2023). URL <https://opg.optica.org/ome/abstract.cfm?uri=ome-13-9-2674>. Publisher: Optica Publishing Group.
- [18] Zhang, C., Zhang, Y. & Jin, G. Continuous modulation of signal polarization in an exciton polariton amplifier. *Journal of Applied Physics* **109**, 053509 (2011). URL <https://doi.org/10.1063/1.3559801>.
- [19] Ghosh, S. & Liew, T. C. H. Quantum computing with exciton-polariton condensates. *npj Quantum Information* **6**, 1–6 (2020). URL <https://www.nature.com/articles/s41534-020-0244-x>. Publisher: Nature Publishing Group.
- [20] Li, X., Lubbers, N., Tretiak, S., Barros, K. & Zhang, Y. Machine learning framework for modeling exciton polaritons in molecular materials. *Journal of Chemical Theory and Computation* **20**, 891–901 (2024). URL <https://doi.org/10.1021/acs.jctc.3c01068>. PMID: 38168674, <https://doi.org/10.1021/acs.jctc.3c01068>.
- [21] Tahir, Z. *et al.* Highly reflective distributed bragg reflectors for planar microcavities: From modelling to experimentation. *Transactions on Electrical and Electronic Materials* **25**, 32–39 (2024). URL <https://doi.org/10.1007/s42341-023-00483-3>.
- [22] Shiau, S.-Y., Eble, B. & Combescot, M. Symmetry breaking for semiconductor excitons induced by Coulomb coupling between heavy and light holes. *Physical Review B* **107**, L081203 (2023). URL <https://link.aps.org/doi/10.1103/PhysRevB.107.L081203>.
- [23] Heckötter, J. Strongly interacting Rydberg excitons in Cu₂O (2020). URL <https://eldorado.tu-dortmund.de/handle/2003/39805>. Accepted: 2020-11-06T08:40:58Z.
- [24] Rommel, P., Main, J., Farenbruch, A., Yakovlev, D. R. & Bayer, M. Exchange interaction in the yellow exciton series of cuprous oxide. *Physical Review B* **103**, 075202 (2021). URL <http://arxiv.org/abs/2102.08900>. ArXiv:2102.08900 [cond-mat].
- [25] Hu, Q. *et al.* Observation of Rydberg moiré excitons. *Science* **380**, 1367–1372 (2023). URL <https://www.science.org/doi/10.1126/science.adh1506>. Publisher: American Association for the Advancement of Science.
- [26] Heckötter, J. *et al.* Asymmetric Rydberg blockade of giant excitons in Cuprous Oxide. *Nature Communications* **12**, 3556 (2021). URL <https://www.nature.com/articles/s41467-021-23852-z>. Publisher: Nature Publishing Group.
- [27] Sliti, N., Fourneau, E., Ratz, T., Touihri, S. & Nguyen, N. D. Mg-doped cu₂o thin films with enhanced functional properties grown by magnetron sputtering under optimized pressure conditions. *Ceramics International* **48**, 23748–23754 (2022). URL <https://www.sciencedirect.com/science/article/pii/S0272884222015814>.
- [28] Kalt, H. & Klingshirn, C. *Semiconductor Optics 1* (Springer Cham, 2019), fifth edn. URL <https://doi.org/10.1007/978-3-030-24152-0>.
- [29] Khramtsov, E. S. *et al.* Radiative decay rate of excitons in square quantum wells: Microscopic modeling and experiment. *Journal of Applied Physics* **119**, 184301 (2016). URL <https://doi.org/10.1063/1.4948664>.
- [30] Toyozawa, Y. Theory of Line-Shapes of the Exciton Absorption Bands. *Progress of Theoretical Physics* **20**, 53–81 (1958). URL <https://doi.org/10.1143/PTP.20.53>.
- [31] Stolz, H., Schöne, F. & Semkat, D. Interaction of Rydberg excitons in cuprous oxide with phonons and photons: optical linewidth and polariton effect. *New Journal of Physics* **20**, 023019 (2018). URL <https://dx.doi.org/10.1088/1367-2630/aaa396>. Publisher: IOP Publishing.

- [32] Elliott, R. J. Intensity of Optical Absorption by Excitons. *Physical Review* **108**, 1384–1389 (1957). URL <https://link.aps.org/doi/10.1103/PhysRev.108.1384>. Publisher: American Physical Society.
- [33] Balewski, J. B. *et al.* Coupling a single electron to a Bose-Einstein condensate. *Nature* **502**, 664–667 (2013). URL <http://arxiv.org/abs/1306.5181>. ArXiv:1306.5181 [physics, physics:quant-ph].
- [34] Schneider, C., Glazov, M. M., Korn, T., Höfling, S. & Urbaszek, B. Two-dimensional semiconductors in the regime of strong light-matter coupling. *Nature Communications* **9**, 2695 (2018). URL <https://www.nature.com/articles/s41467-018-04866-6>. Publisher: Nature Publishing Group.
- [35] Novotny, L. Strong coupling, energy splitting, and level crossings: A classical perspective. *American Journal of Physics* **78**, 1199–1202 (2010). URL <https://doi.org/10.1119/1.3471177>.
- [36] S. Dovzhenko, D., V. Ryabchuk, S., P. Rakovich, Y. & R. Nabiev, I. Light-matter interaction in the strong coupling regime: configurations, conditions, and applications. *Nanoscale* **10**, 3589–3605 (2018). URL <https://pubs.rsc.org/en/content/articlelanding/2018/nr/c7nr06917k>. Publisher: Royal Society of Chemistry.
- [37] Rodriguez, S. R.-K. Classical and quantum distinctions between weak and strong coupling. *European Journal of Physics* **37**, 025802 (2016). URL <https://dx.doi.org/10.1088/0143-0807/37/2/025802>. Publisher: IOP Publishing.
- [38] Moretti, S. Classical Mechanics Ch 6 Coupled Oscillators. URL <https://www.southampton.ac.uk/~stefano/courses/PHYS2006/chapter6.pdf>.
- [39] Wang, T.-T., Laude, V., Kadic, M., Wang, Y.-F. & Wang, Y.-S. Complex-Eigenfrequency Band Structure of Viscoelastic Phononic Crystals. *Applied Sciences* **9**, 2825 (2019). URL <https://www.mdpi.com/2076-3417/9/14/2825>. Number: 14 Publisher: Multidisciplinary Digital Publishing Institute.
- [40] Deng, H., Haug, H. & Yamamoto, Y. Exciton-polariton Bose-Einstein condensation. *Reviews of Modern Physics* **82**, 1489–1537 (2010). URL <https://link.aps.org/doi/10.1103/RevModPhys.82.1489>. Publisher: American Physical Society.
- [41] Hopfield, J. J. Theory of the Contribution of Excitons to the Complex Dielectric Constant of Crystals. *Physical Review* **112**, 1555–1567 (1958). URL <https://link.aps.org/doi/10.1103/PhysRev.112.1555>. Publisher: American Physical Society.
- [42] Tokunaga, E., Ivanov, A. L., Nair, S. V. & Masumoto, Y. Hopfield coefficients measured by inverse polariton series. *Physical Review B* **63**, 233203 (2001). URL <https://link.aps.org/doi/10.1103/PhysRevB.63.233203>. Publisher: American Physical Society.
- [43] Erkensten, D., Brem, S. & Malic, E. Exciton-exciton interaction in transition metal dichalcogenide monolayers and van der waals heterostructures. *Phys. Rev. B* **103**, 045426 (2021). URL <https://link.aps.org/doi/10.1103/PhysRevB.103.045426>.
- [44] Zhang, W. *et al.* Steering room-temperature plexcitonic strong coupling: A diexcitonic perspective. *Nano Letters* **21**, 8979–8986 (2021). URL <https://doi.org/10.1021/acs.nanolett.1c02248>.
- [45] Shahnazaryan, V., Iorsh, I., Shelykh, I. A. & Kyriienko, O. Exciton-exciton interaction in transition-metal dichalcogenide monolayers. *Phys. Rev. B* **96**, 115409 (2017). URL <https://link.aps.org/doi/10.1103/PhysRevB.96.115409>.
- [46] Subedi, I. *Optical Evaluation and Simulation of Photovoltaic Devices for Thermal Management*. Ph.D. thesis, United States – Ohio (2019). URL <https://www.proquest.com/dissertations-theses/optical-evaluation-simulation-photovoltaic/docview/2323127736/se-2?accountid=8312>. Copyright - Database copyright ProQuest

LLC; ProQuest does not claim copyright in the individual underlying works.

- [47] Mackay, T. G. & Lakhtakia, A. *The Transfer-Matrix Method in Electromagnetics and Optics*. Synthesis Lectures on Electromagnetics (Springer International Publishing, Cham, 2020). URL <https://link.springer.com/10.1007/978-3-031-02022-3>.
- [48] Troparevsky, M. C., Sabau, A. S., Lupini, A. R. & Zhang, Z. Transfer-matrix formalism for the calculation of optical response in multilayer systems: from coherent to incoherent interference. *Optics Express* **18**, 24715–24721 (2010). URL <https://opg.optica.org/oe/abstract.cfm?uri=oe-18-24-24715>. Publisher: Optica Publishing Group.
- [49] Fowles, G. *Introduction to Modern Optics* (Dover Publications, New York, 1975), second edn. URL <https://store.doverpublications.com/products/9780486659572>.
- [50] Mohammed, Z. H. The Fresnel Coefficient of Thin Film Multilayer Using Transfer Matrix Method TMM. *IOP Conference Series: Materials Science and Engineering* **518**, 032026 (2019). URL <https://dx.doi.org/10.1088/1757-899X/518/3/032026>. Publisher: IOP Publishing.
- [51] Heald, M. & Marion, J. *Classical Electromagnetic Radiation* (Saunders College, 1995), 3rd edn. URL <https://works.swarthmore.edu/fac-physics/196>.
- [52] Ware, M. & Peatross, J. *Physics of Light and Optics (Black & White)* (Lulu.com, 2015). Google-Books-ID: Cw2LDwAAQBAJ.
- [53] Paschotta, D. R. Bragg mirrors. URL <https://www.rp-photonics.com/bragg-mirrors.html>.
- [54] Keskar, D. Reflectivity simulation by using transfer matrix method - IOPscience. In *ICRFS* (Nagpur, India, 2021). URL <https://iopscience.iop.org/article/10.1088/1742-6596/1913/1/012051>.
- [55] Kumar, R. Design and optimization of dielectric dbr for vcsel, targeting emission range of 520-550 nm. *e Department of Electrical Engineering at the Indian Institute of Technology, Bombay* (2019).
- [56] Schöne, F., Stolz, H. & Naka, N. Phonon-assisted absorption of excitons in Cu_2O . *Physical Review B* **96**, 115207 (2017). URL <https://link.aps.org/doi/10.1103/PhysRevB.96.115207>. Publisher: American Physical Society.
- [57] Schöne, F. Optical Properties of yellow Excitons in Cuprous Oxide (2017). URL https://rosdok.uni-rostock.de/file/rosdok_disshab_0000001908/rosdok_derivate_0000044476/Dissertation_Schoene_2018.pdf.
- [58] Misra, P. K. Chapter 2 - Phonons and Lattice Vibrations. In Misra, P. K. (ed.) *Physics of Condensed Matter*, 37–69 (Academic Press, Boston, 2012). URL <https://www.sciencedirect.com/science/article/pii/B9780123849540000025>.
- [59] Elliott, R. J. Polarons and Excitons. *Physical Review* **108**, 269 (1957).
- [60] Saba, M. *et al.* Correlated electron-hole plasma in organometal perovskites. *Nature Communications* **5**, 5049 (2014). URL <https://www.nature.com/articles/ncomms6049>. Publisher: Nature Publishing Group.
- [61] Ravichandiran, C. *et al.* Effect of deposition temperature on key optoelectronic properties of electrodeposited cuprous oxide thin films. *Optical and Quantum Electronics* **50**, 281 (2018). URL <https://doi.org/10.1007/s11082-018-1531-z>.
- [62] Ujihara, Y. H., Kikuo (ed.) *Spontaneous Emission and Laser Oscillation in Microcavities* (CRC Press, London, 2020).
- [63] Kavokin, A. V., Sheremet, A. S., Shelykh, I. A., Lagoudakis, P. G. & Rubo, Y. G. Exciton-photon correlations in bosonic condensates of exciton-polaritons. *Scientific Reports* **5**, 12020 (2015). URL <https://www.nature>.

[com/articles/srep12020](https://www.nature.com/articles/srep12020). Publisher: Nature Publishing Group.

- [64] Ferreira, B., Rosati, R., Fitzgerald, J. M. & Malic, E. Signatures of dark excitons in exciton–polariton optics of transition metal dichalcogenides. *2D Materials* **10**, 015012 (2022). URL <https://dx.doi.org/10.1088/2053-1583/aca211>.
- [65] Wall, F., Mey, O., Schneider, L. M. & Rahimi-Iman, A. Continuously-tunable light–matter coupling in optical microcavities with 2D semiconductors. *Scientific Reports* **10**, 8303 (2020). URL <https://www.ncbi.nlm.nih.gov/pmc/articles/PMC7237431/>.
- [66] Bender, C. Basics of PT Symmetry. In *PT Symmetry: In Quantum and Classical Physics*, 3–38 (WORLD SCIENTIFIC (EUROPE), 2019). URL https://doi.org/10.1142/9781786345967_fmatter.
- [67] Romeira, B. & Fiore, A. Purcell effect in the stimulated and spontaneous emission rates of nanoscale semiconductor lasers. *IEEE Journal of Quantum Electronics* **54**, 1–12 (2018).
- [68] Cristofolini, P. Optical control of polariton condensation and dipolaritons in coupled quantum wells (2015). URL <https://www.repository.cam.ac.uk/handle/1810/247219>.
- [69] Bhuyan, R., Lednev, M., Feist, J. & Börjesson, K. The effect of the relative size of the exciton reservoir on polariton photophysics. *Advanced Optical Materials* **12**, 2301383 (2023). URL <https://onlinelibrary.wiley.com/doi/abs/10.1002/adom.202301383>. <https://onlinelibrary.wiley.com/doi/pdf/10.1002/adom.202301383>.
- [70] Adams, C. S., Pritchard, J. D. & Shaffer, J. P. Rydberg atom quantum technologies. *Journal of Physics B: Atomic, Molecular and Optical Physics* **53**, 012002 (2019).
- [71] Sakaguchi, A. *et al.* Nonlinear feedforward enabling quantum computation. *Nature Communications* **14**, 3817 (2023). URL <https://doi.org/10.1038/s41467-023-39195-w>.
- [72] Walther, V., Grünwald, P. & Pohl, T. Controlling Exciton-Phonon interactions via electromagnetically induced transparency. *Phys Rev Lett* **125**, 173601 (2020).
- [73] Makhonin, M. *et al.* Nonlinear rydberg exciton-polaritons in cu2o microcavities. *Light: Science & Applications* **13**, 47 (2024). URL <https://doi.org/10.1038/s41377-024-01382-9>.
- [74] Peyronel, T. *et al.* Quantum nonlinear optics with single photons enabled by strongly interacting atoms. *Nature* **488**, 57–60 (2012). URL <https://doi.org/10.1038/nature11361>.

A Data availability

The data for [3] is available [here](#).

B Code availability

The code for this project is submitted separately.